

Imaging Atoms in Regular Structures via High Harmonic Generation

Noah Welikson

B.S. Engineering Physics

University of Colorado Boulder

Thesis Advisor

Andreas Becker, JILA and Department of Physics

Thesis Committee

Andreas Becker, JILA and Department of Physics

Jun Ye, JILA and Department of Physics

Jonathan Wise, Department of Mathematics

March 18th, 2024

Acknowledgment

I would like to first extend my gratitude to my advisor, Doctor Andreas Becker for his guidance, patience and support. Under his direction I solidified my passion and discovered my confidence in doing physics. Doctor Becker gave me the space to find my footing in science while always being available to answer my questions on my own research and career in physics. I would also like to thank the rest of the Ultrafast Theory Group for their continued support, liveliness, and interest in my development as a physicist. I will always look back fondly on my two years working with you all. I would also like to especially thank Spencer Walker for his mentorship and time spent answering hours of questions, as well as Nicholas Jenkins for sharing his time and resources on coherent diffractive imaging.

This work was supported by the National Science Foundation (Award No. PHY-2317149)

TABLE OF CONTENTS

List of Figures	iv
Chapter 1: Introduction	1
1.1 Motivation	1
1.2 Background	3
1.2.1 Optical Theory	3
1.2.2 Macroscopic Considerations	9
1.2.3 Image Generation	11
Chapter 2: Methods	15
2.1 Propagation of Radiation	15
2.2 Diffractive Imaging	15
2.3 Phase Retrieval	16
2.3.1 The Hybrid Input Output Method	16
2.3.2 The Difference Map Method	17
2.3.3 Optical Lattice Supports	18
Chapter 3: Results with Static Support	19
Chapter 4: Dynamic support	23
4.1 Shrink Wrapping: Concept and Implementation	23
4.2 Results with Shrink Wrapping	25

Chapter 5: Outlook	30
5.1 3D Imaging	30
5.1.1 Diffraction Volumes	30
5.1.2 Computational Considerations	32
5.2 Strong Field Approximation	33
5.2.1 The Stationary Phase Approximation	34
References	38

LIST OF FIGURES

1.1	HHG spectrum generated from hydrogen atom interacting with a 20 cycle laser pulse at a wavelength of 800 nm and a peak intensity of 10^{14}W/cm^2	6
1.2	Diagram of Multiphoton Ionization. Many photons with $\hbar\omega < I_p$ are absorbed both above and below the ionization threshold	8
1.3	Diagram of semiclassical HHG including tunnel ionization from the ground state, propagation in the continuum and recollision and photoemission, (taken from Popmintchev et. al. [10])	9
1.4	Diffraction pattern of the 7th harmonic generated by a 10x10 grid of hydrogen atoms with 300nm interatomic spacing interacting with the field of an 800nm Gaussian beam of peak intensity 10^{14}W/cm^2 . k_x and k_y are in units of inverse wavelength.	12
1.5	Diagram of coherent diffraction imaging experimental setup, (taken from the UCLA Coherent Imaging Group) [16]	13
1.6	Diagram of phase reconstruction algorithm, (taken from the UCLA Coherent Imaging Group) [16]	14
2.1	Real space support for phase reconstruction in an optical lattice.	18
3.1	Reconstructed images for optical lattices with different number of lattice sites filled using the image generated by the seventh harmonic. From left to right; 96 filled sites, 47 filled sites, 9 filled sites	20
3.2	Phase reconstruction of a 1D lattice of 10 hydrogen atoms using the 7th harmonic and a Difference Map method with static support. Shown are the diffraction data (a), the magnitudes of the true real space data taken as the inverse Fourier transform of the diffraction data with phase (b), final reconstruction (c) and static support of a bounding box around the optical lattice (d), and the error over iterations (e)	21
3.3	Same as Figure 3.2 but for a 2D lattice of 10×10 hydrogen atoms.	22

4.1	Phase reconstruction of gold pellets with shrink wrapping. (a) The diffraction pattern of the object. (b,c,d) Evolution of reconstruction and support with shrink wrapping with the left inset being the reconstruction at the iteration and the right inset being the support. The quality of the reconstruction increases substantially as the support grows tighter to the gold pellets seen in (d) (taken from Marchesini et al. [21]).	24
4.2	Reconstructions of a 10×10 lattice of hydrogen atoms in three different regimes with 300 nm interatomic spacing using the seventh harmonic with a Difference Map method and Shrink Wrapping.	25
4.3	Reconstruction behaviour over time for a 1D lattice of 9 hydrogen atoms using the seventh harmonic and a Difference Map method with Shrink Wrapping including the error over time (top row), reconstruction over time (middle row), and support over time (bottom row)	26
4.4	Same as Figure 4.3 for a 2D lattice of 53 hydrogen atoms.	27
4.5	Phase reconstruction of 1D lattice with one empty site.	28
5.1	Schematic layout of 3D X-ray diffraction (taken from H. Jiang et al. [22]).	31

CHAPTER 1

INTRODUCTION

1.1 Motivation

Throughout history many of the most significant advancements in science led to new ways of probing smaller and smaller into the world around us. By developing the first high magnification lenses Hooke and Leeuwenhoek were able to discover the nature of the microscopic world teeming with life [1], Geiger and Mardsen discovered the structure of the atom in 1908 by scattering alpha particle off of gold plates [2], and the Standard Model was confirmed in 2013 with the detection of the Higgs Boson using the high powered scattering experiments at the Large Hadron Collider [3].

Throughout the sciences, and especially in physics, microscopy has been a nearly universal tool for probing deeper into the systems we are interested in. Improving the resolution of these microscopes, how small of an object we can make out, has thus been an ongoing area of research for nearly 500 years. In 1873 Ernst Abbe placed the lower limit of the resolution of a microscope at one half the illuminating wavelength [4]. In effect, the way to probe smaller is then to reduce the wavelength of illumination. Since then significant resources have been focused into research how develop lower and lower wavelength microscopes.

Today, the state of the art is to employ extreme ultra violet (EUV) to soft x-Ray wavelengths to obtain nanometer scale resolution. These wavelengths have lead to a range of important scientific discoveries including revealing the structure of DNA in 1953. However using these wavelengths poses some issues; (1) the high photon energy of the scattered light means that conventional lenses can not be fabricated without being damaged or distorted, (2) until recently coherent X-ray sources have been extremely difficult to come by, requiring expensive and non-portable techniques such as free electron laser and synchrotrons [5].

First addressing (1), many alternative lenses have been developed to deal with the high photon energies including refractive Lenses, Fresnel Zone plates, reflective optical components, and multilayer Lau lenses, in order to refocus scattered X-rays back into an image. However, all of these techniques depend highly on the fabrication quality and precision of the lenses involved [5].

Instead one can forgo these these physical challenges that come along with lens construction by transferring the focusing operation from a lens to a computer algorithm. This is the technique used in Coherent

Diffraction Imaging (CDI). Instead of scattered light being refocused into an image using a lens, scattered light is collected on a detector, and an algorithm is used to "virtually refocus" the scattered light.

To address (2), recent developments in intense laser generation ($10^{14}W/cm^2$) have allowed for high harmonic generation (HHG). It is a process whereby intense infrared lasers, which are more readily accessible, drive the generation of high frequency coherent light by interacting with atoms in a gas jet. These developments have led to an explosion in table top ready sources of EUV and soft X-ray light [6]. The application of HHG for imaging purposes works by filtering one of the higher frequency components generated during this process, and then refocusing this coherent light back into a beam for microscopy.

By combining HHG EUV sources with CDI techniques, researchers have developed a table top system for performing extremely high resolution imaging. While much work has already been done in using HHG light as a source of illumination, in this thesis we instead explore extensions of these ideas by considering the use of the high harmonic generation process itself as the platform for microscopy. In order to explore this technique we attempt to evaluate the effectiveness of this type of imaging. More specifically we determine how much information the interference pattern of HHG light emitted from different atoms contains about the relative position of the atoms, i.e. does such a light pattern provide an image of the source of the emitted light. To test this idea, we consider that the atoms, that generate the high harmonics, are distributed regularly. Thus, instead of a gas jet with irregular distribution of atoms in typical high harmonic generation set-ups we consider a regular pattern of atoms, which will allow us to more exactly determine the effectiveness and precision of this technique - a potential experimental realization of such a regular pattern could be an optical lattice.

Thus the goal of this thesis is to explore the possibility to reconstruct an image of the source, i.e. the regular distribution of the atoms, and ways to improve the quality of the image. In order to focus on these questions, we neglect a few aspects that would impact the experimental realization of the approach: We assume that the conversion efficiency of HHG is 1, i.e. every atom in the lattice is producing high harmonics. In reality the conversion efficiency would be on the order of 10^{-2} to 10^{-3} . More careful thought would need to be given to this issue to employ the method experimentally, however this is beyond the scope of this thesis.

1.2 Background

1.2.1 Optical Theory

In order to perform any type of analysis of the macroscopic dynamics of HHG in optical lattices, we must first understand microscopic and macroscopic aspects of the generation of high-order harmonics in a set of atoms. To this end, we start by considering the three components of the microscopic dynamics of the interaction between atoms and the electric field of an intense laser field: the atomic nucleus and the electron.

We first note that because the mass of the atomic nucleus is much larger than that of the electrons, the dynamics of the nucleus and the electrons can be evaluated separately [7]. Operationally, this means that the electronic dynamics happen quickly enough relative to the nuclear dynamics that we can consider the nucleus fixed at the origin of our system.

We begin by considering the wave functions of each individual electron in these systems. Each electron experiences the Coulomb potential by the nucleus as well as by all the other electrons in the atom. This produces the total potential seen in Equation (1.1), for the j 'th electron.

$$V_{Atomic,Single} = \sum_{i=1, i \neq j}^n \frac{-e}{|\vec{r}_j - \vec{r}_i|} + \frac{Ze}{|\vec{r}_j|} \quad (1.1)$$

where e is the charge of the electron, Z is the number of protons in the nucleus, n is the number of other electrons, \vec{r}_j is the position of the j 'th electron, and \vec{r}_i is the position of the i 'th electron in the atom all relative to the nucleus at the origin.

Considering the laser interaction potential, we note that it is given via the field $\vec{E}(t, r)$ of the laser. From classical electrodynamics we recognize that the electric potential is given via the dipole potential $V_{dipole} = -\vec{E} \cdot \vec{r}$. Therefore, we find the following laser interaction potential.

$$V_{Laser} = -\vec{E}(t) \cdot \vec{r} \quad (1.2)$$

We therefore have the Hamiltonian for each individual electron as follows:

$$H_{Single} = -\hbar^2 \frac{p^2}{2m} + V_{Atomic,Single} + V_{Laser} = -\hbar^2 \frac{\nabla^2}{2m} + \sum_i^n \frac{-e}{|\vec{r} - \vec{r}_i|} + \frac{Ze}{|\vec{r}|} - \vec{E} \cdot \vec{r} \quad (1.3)$$

and the total Hamiltonian for the system, including all of the electrons, is the sum over all of these single

electron Hamiltonians, and we find the total Hamiltonian

$$H_{total} = \sum_j^n \left[-\hbar^2 \frac{\nabla_j^2}{2m} + \sum_{j \neq i} \frac{-e}{|\vec{r}_i - \vec{r}_j|} + \frac{Ze}{|\vec{r}_j|} - \vec{E} \cdot \vec{r}_j \right] \quad (1.4)$$

Resolving the dynamics of this system can become incredibly complicated since we must solve for the dynamics of each electron in the electric field of an intense laser field, leading to a wave function with a large number of dimensions corresponding to the large number of degrees of freedom of the system. Numerically solving the Schrödinger equation for relatively simple systems can already be computationally expensive, and so fully modeling the dynamics of a large number of electrons can become computationally intractable.

The Single Active Electron Approximation

In order to reduce the dimensionality of the problem we employ the single active electron approximation (SAE). Under the SAE we assume that the laser field only interacts with the most weakly bound electron in an atom, while the other electrons act as frozen spectators [8]. Under this approximation we only need to consider the evolution of one electron wave function, and the Hamiltonian reduces to

$$H_{SAE} = -\hbar^2 \frac{\nabla^2}{2m} + V_{SAE} - \vec{E}(t) \cdot \vec{r} \quad (1.5)$$

where V_{SAE} is some modified potential representing the contributions of both the nucleus and the spectator electrons. Determining an approximate form of these potentials is an ongoing area of research, however the calculations in this thesis were all carried out using the hydrogen atom. In this case there is only one electron to consider, and V_{SAE} reduces to a simple Coulomb potential. In principal, the procedure presented in this thesis can be used to model systems with any type of atom provided the appropriate V_{SAE} is used.

Solving the TDSE

We now consider the electronic wave function, $\Psi(\vec{r}, t)$ which is given by the solution of the time dependent Schrödinger equation below:

$$H_{SAE}(t)\Psi(\vec{r}, t) = i\hbar \frac{\partial}{\partial t} \Psi(\vec{r}, t) \quad (1.6)$$

In general, there is no analytic solution for $\Psi(\vec{r}, t)$ in a time varying electric field $\vec{E}(t)$ and Coulombic

potential and thus the TDSE must be solved numerically. A full description of these numerical methods is beyond the scope of this thesis but a general outline is given below. We begin at $t = 0$ with the electron in the ground state of the atomic potential. To find this ground state wavefunction we solve the time-independent Schrödinger equation:

$$H\Psi(r) = [-\hbar^2 \frac{\nabla^2}{2m} + V_{SAE}] \Psi(\vec{r}) = E\Psi(\vec{r}) \quad (1.7)$$

For the hydrogen atom with $V_{SAE} = \frac{e}{|\vec{r}|}$ these states are known exactly. For more complex potentials an exact solution is unlikely to be found, and instead methods such as perturbation theory or numerical solutions are employed to determine the ground state [9].

Next, we notice that the time dependent Schrödinger equation can be rewritten as follows:

$$\Psi(\vec{r}, t) = e^{-\frac{i}{\hbar} \int_0^t H_{SAE} dt} \Psi(\vec{r}, 0) \quad (1.8)$$

Which transforms the differential equation into an integral equation which is more tractable for numerical computation. Taking a small interval in time Δt we find the following equation for the evolution of the wave function at each step in time.

$$\Psi(r, t + \Delta t) = e^{-\frac{i}{\hbar} H_{SAE} \Delta t} \Psi(r, t) \quad (1.9)$$

and the Crank-Nicolson method can then be used to calculate $\Psi(r, t_i)$ for each time step t_i with $\Psi(r, 0)$ taken as the ground state calculated previously.

HHG Spectra

Next we use the solution for $\Psi(r, t)$ to analyze the light generated in these laser-atom interactions. From classical electrodynamics we know that the field radiated in this system should be proportional to the dipole acceleration. The dipole operator in quantum mechanics follows a similar form to classical electrodynamics with $\vec{d} = e\vec{r}$. Therefore, we find the expectation value of the generated light as follows:

$$E_{rad}(t) \propto \frac{d^2}{dt^2} \langle \Psi(r, t) | \vec{d} | \Psi(r, t) \rangle \propto \frac{d^2}{dt^2} \int dV \Psi^*(r, t) \vec{r} \Psi(r, t) \quad (1.10)$$

We can then compute the spectrum of the radiation as the Fourier transform of the electric field in the

time domain

$$P(\omega) = |\mathcal{F}(E_{rad}(t))| \quad (1.11)$$

where $P(\omega)$ is the intensity of the emitted radiation. By carrying out the procedure outlined previously using an intense periodic laser field $\vec{E}(t)$ one calculates the spectrum, a typical result of such a calculation is shown in Figure 1.1.

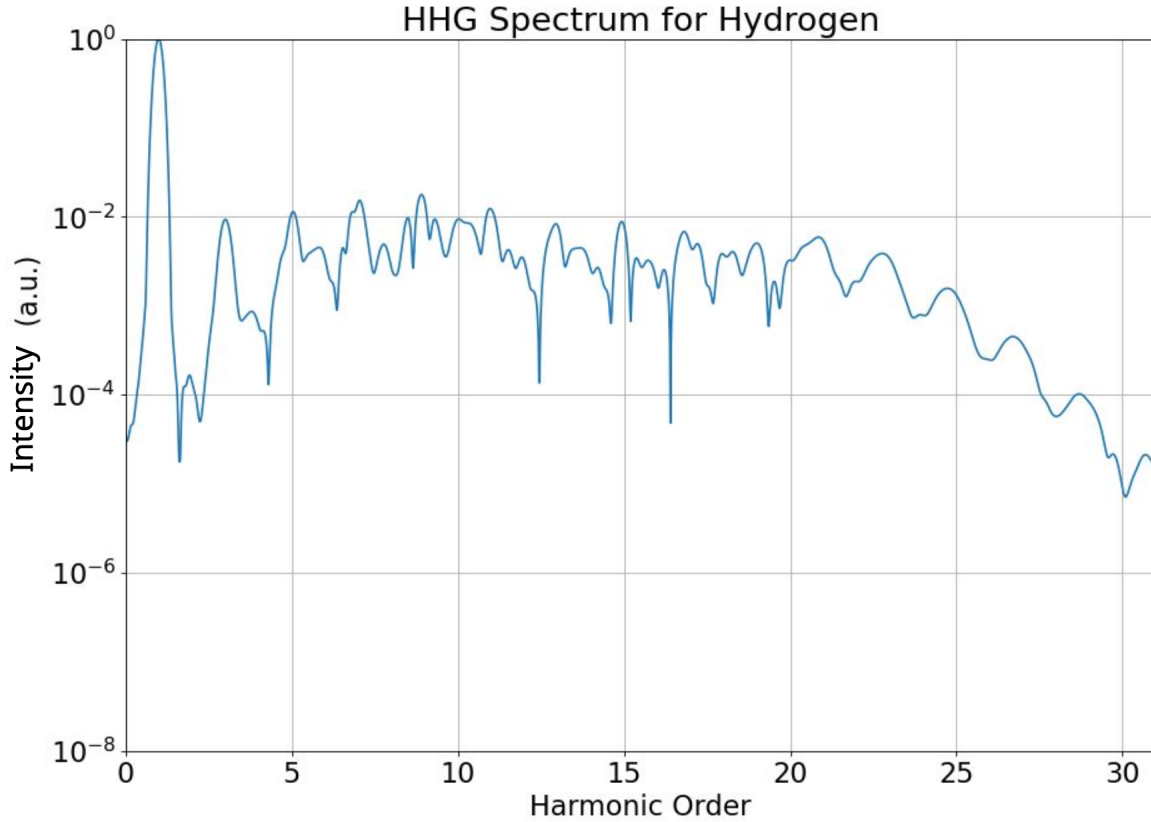


Figure 1.1: HHG spectrum generated from hydrogen atom interacting with a 20 cycle laser pulse at a wavelength of 800 nm and a peak intensity of 10^{14}W/cm^2

High Harmonic Generation: Heuristic Description

A description of HHG that provides a good intuition for why we see observe intense harmonics during the interaction of strong field radiation with atoms can be given based on the uncertainty relation between energy and time. Beginning with the discrete energy levels of the electrons in an atom, we know each electron has an ionization energy I_p . In the presence of a relatively weak field we know that the electron is likely not to ionize unless it absorbs a photon with frequency ω such that its energy $\hbar\omega > I_p$ at which point the electron

will be emitted with kinetic energy $E = I_p - \hbar\omega$ in accordance with the photoelectric effect as described by Einstein. This is due to the fact that the electron should only be promoted to an energy eigenstate, which are separated into discrete bound states below the ionization energy, and then a continuum above the ionization energy. Therefore, the electron will only be seen to be ionized into the continuum if it absorbs a photon with energy larger than the ionization energy.

However, we know from Heisenberg's uncertainty principle that there is an uncertainty relation between time and energy.

$$\Delta E \Delta t \geq \frac{\hbar}{2} \quad (1.12)$$

Therefore we may be able to excite an electron with the absorption of a photon with energy $\Delta E < I_p$ above the ground state for some amount of time Δt into a so called a "virtual energy state". In general, this Δt will be very small; an estimate shows that for a photon of an $800nm$ laser Δt will be on the order of $10^{-16}s$. This means there is a time window of about $10^{-16}s$ for meaningful interactions with the electron in this state to occur. A weak field has a relatively low photon density and it is unlikely another photon will interact with the electron during this window. However for a strong field and high photon density it is much more likely another photon will be absorbed by the electron within this time window. At this point the electron will be further excited into a virtual energy state with $\Delta E = 2\hbar\omega$. This can occur N times with the electron absorbing N photons in a process called multi photon ionization which is sketched in Figure 1.2 .

The electron now has absorbed an energy $N\hbar\omega$ and is in some continuum state. It then can transition with some probability back into the ground state. If the electron should recollide with its parent nucleus (recombination with the ground state) the atom will photo-emit a single photon of the kinetic energy $N\hbar\omega$. Therefore we should expect the radiation spectrum emitted from the atom to feature more intense peaks at integer multiples of the laser frequency, which explains the peak structure in the spectra calculated from the TDSE in Figure 1.1. However an important feature of HHG is the fact that these harmonics are generated coherently with the driving laser, which is not as easily explained in the picture described above. To explain this we instead turn to what is called the semiclassical model.

In the semiclassical model we consider a bound electron in the ground state of its parent nucleus. A classical laser field is then turned on, "tipping" the Coulomb potential of the nucleus and allowing the electron to tunnel ionize out of the bound state. After which we then consider the classical motion of the electron in the continuum only under the influence of the laser field. The electron is first accelerated by

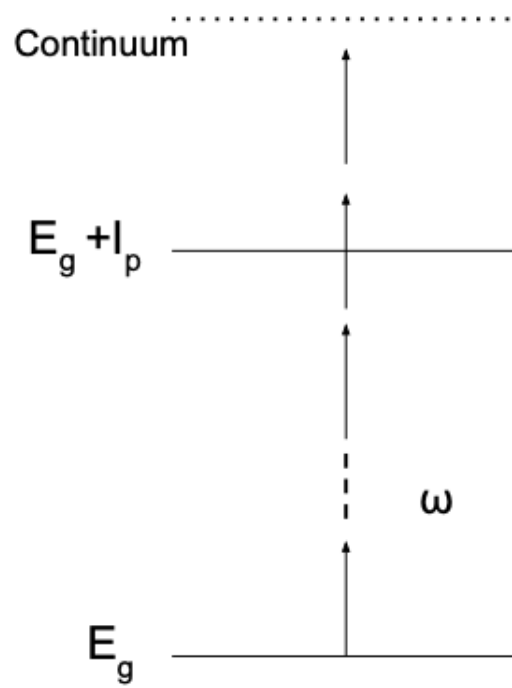


Figure 1.2: Diagram of Multiphoton Ionization. Many photons with $\hbar\omega < I_p$ are absorbed both above and below the ionization threshold

the laser field away from the nucleus before the laser field drives the electron back down to the parent nucleus. Upon return to the parent nucleus, with a certain probability the electron recombines with the nucleus under the emission of a single photon (see Figure 1.3). This gives a justification for why HHG spectra are generated coherently with the driving laser, since the electron dynamics including ionization, propagation, and recollision are all driven coherently with the laser. We will return to this model later in this thesis when considering calculating HHG spectra in macroscopic samples.

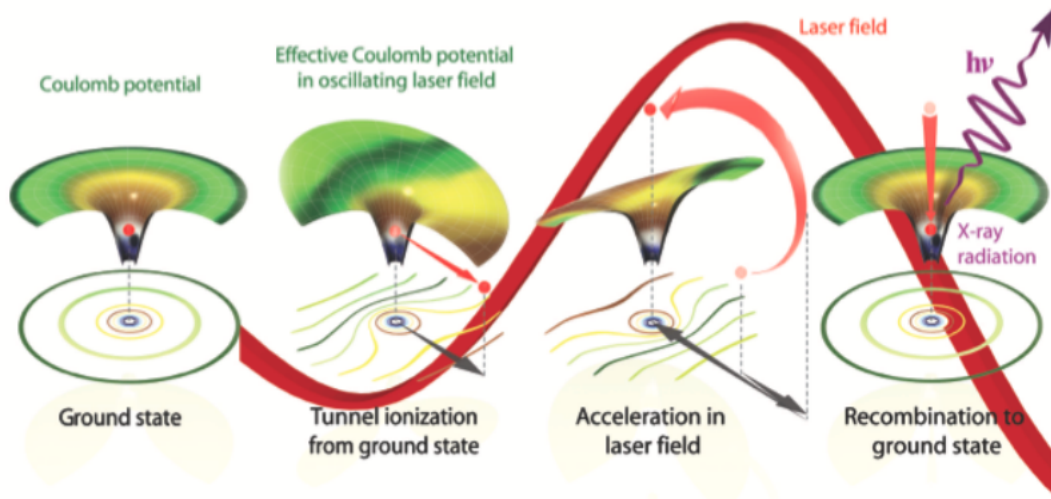


Figure 1.3: Diagram of semiclassical HHG including tunnel ionization from the ground state, propagation in the continuum and recollision and photoemission, (taken from Popmintchev et. al. [10])

1.2.2 Macroscopic Considerations

We are now ready to begin considering the HHG spectra produced by an arrangement of many atoms, such as those in an optical lattice. In general optical lattices will feature arrays of laser trapped atoms with lattice spacing on the order of hundreds of nanometers of separation [11]. Because the interatomic distance is large we approximate that there are no atom-atom interactions and the atomic dynamics within the lattice are determined solely by interactions with the fundamental laser field [12]. This means that we may consider the dynamics of each atom individually without considering perturbations to the Hamiltonian in Equation (1.5) [13]. The arrangements we consider in this thesis will have on the order of 100 atoms. Therefore although full single-atom TDSE calculations can be computationally expensive, the relatively small number of atoms means that carrying out these full TDSE calculations is still practical. To carry out these calculations we define some space and time dependent laser field $\vec{E}(\vec{r}, t)$. Then for the interaction with an individual atom

we reduce this laser field to its time dependent component at the atom's position which gives a purely time dependent field $\vec{E}_r(t)$. In general, the beam width of the lasers used in HHG experiments will be on the order of tens of microns [12], much larger than the spatial range of the electron dynamics we are concerned with. Therefore, the spatial dependence of the laser experienced by each individual electron will be approximately constant. This allows us to use the spatially independent $\vec{E}_r(t)$ when calculating the spectra for each atom by performing TDSE calculations as discussed above.

In order to generate an image, we will need to find the field generated from these radiating atoms at some far field detector. This can be calculated as the superposition of the fields generated from each atom individually. Therefore, we need to propagate the radiation from each atom to some far field point and then add all these fields together. For each atom this can be calculated as follows:

$$E(r_d, \omega) = \frac{1}{c^2 |r_d|} e^{-i\frac{\omega}{c}|r_d|} a(\omega) e^{-i\frac{\omega}{c} r_j \cdot (\hat{r}_d - \hat{s}_L)} \hat{p}_L \quad (1.13)$$

where \vec{r}_d is the location of the detector, \vec{r}_j is the location of the atom, $a(\omega)$, is the dipole acceleration in the frequency domain as discussed previously, \hat{s}_L is the laser propagation direction, and \hat{p}_L is the laser polarization direction. Noticing that the first phase factor in the equation above depends only on the distance to the detector we can factor it out to arrive at the equation for the macroscopic spectrum at a far field point [13, 12]:

$$E(r_d, \omega) \propto \sum_j a_j(\omega) e^{-i\frac{\omega}{c} r_j \cdot (\hat{r}_d - \hat{s}_L)} \hat{p}_L \quad (1.14)$$

where j is the index of each atom. We note that factoring out the phase associated with the detector distance forces all the points on the detector to have the same distance from the origin, which will allow us to further simplify the expression. By using that $|r_d|$ is equal for all detector points we can pull out the complex factor in front of the sum in Equation (1.14) so that we only need to consider the relative positions of the atoms to each other, and their relative angle to the detector. This corresponds to sampling a hemispherical detector around the sample. We can now characterize the coordinates of the detector points entirely by the polar angle θ and the radial angle ϕ relative to the z axis. Furthermore, we arbitrarily choose the laser to be propagating in the z direction and polarized in the y direction to get

$$r_d(\theta, \phi) = \sin(\theta) \cos(\phi) \hat{x} + \sin(\theta) \sin(\phi) \hat{y} + \cos(\theta) \hat{z} \quad (1.15)$$

Inserting into Equation (1.14) we get

$$E(\theta, \phi, \omega) \propto \sum_j a_j(\omega) e^{-i\frac{\omega}{c}(r_{dx} \sin(\theta) \cos(\phi) + r_{dy} \sin(\theta) \sin(\phi))} \hat{r}_d \quad (1.16)$$

By sampling over θ and ϕ we generate the far field angle-resolved diffraction pattern. In order to transform the angle resolved data to Cartesian resolved data we recognize that in the far field the macroscopic radiation from the sample is approximately normal to the surface of the hemispherical detector. Therefore, we can take the x and y components of the radiation field at each detector point:

$$E_x(\theta, \phi, \omega) = \sin(\theta) \cos(\phi) E(\theta, \phi, \omega) \quad (1.17)$$

$$E_y(\theta, \phi, \omega) = \sin(\theta) \sin(\phi) E(\theta, \phi, \omega) \quad (1.18)$$

This corresponds to projecting the diffraction data over a unit sphere onto the unit disk. However, in a real experiment the detector loses all access to the phase information contained in this data and sees only the modulus of E_x and E_y . This produces a diffraction image such as the one shown in Figure 1.4.

1.2.3 Image Generation

We now wish to recover information about the sample we are interested in from this diffraction image. One may notice that Equation (1.14) looks very similar to a discrete Fourier transform, and indeed in the field of diffractive imaging one considers these far field diffraction patterns to be Fourier transforms of the near field image of the object [14, 15]. In Coherent Diffractive Imaging (CDI) a beam of coherent light is scattered off an object to produce a diffraction image like the one in Figure 1.4 using a setup shown in Figure 1.5. An important difference between CDI and the method being explored in this thesis is that the images produced in this thesis are generated directly from HHG radiation rather than scattering light off of atoms. While conventional CDI will generally only use one frequency of light, HHG radiation gives us access to the entire frequency range of an HHG spectrum. In effect this means that one experiment will generate a range of diffraction images across the HHG spectrum. Regardless, we can pick out a diffraction image related to one of these frequencies leaving the following process almost exactly analogous to CDI.

Knowing that the far field diffraction image should be the Fourier transform of the near field image, we may wish to simply take the inverse Fourier transform to recover a near field image of our object. However,

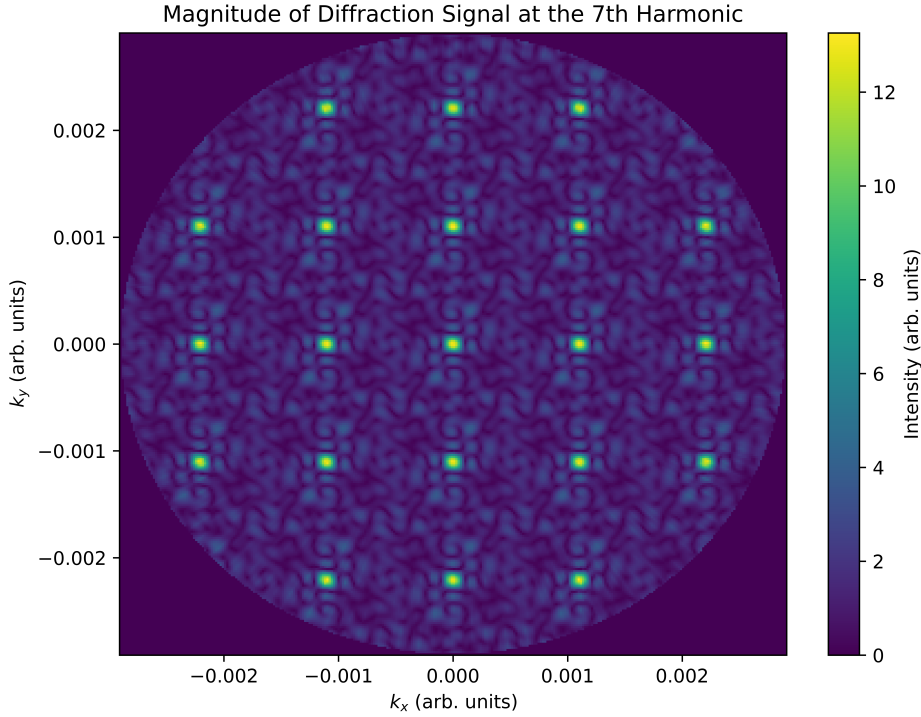


Figure 1.4: Diffraction pattern of the 7th harmonic generated by a 10x10 grid of hydrogen atoms with 300nm interatomic spacing interacting with the field of an 800nm Gaussian beam of peak intensity 10^{14} W/cm². k_x and k_y are in units of inverse wavelength.

in reality a detector will only see the intensity of the diffraction data, and all the phase information will be lost. This is problematic since there are many possible configurations of the object in the near field, $\rho(r)$, which we will henceforth call "real space," that could produce the diffraction intensities in the far field, $\rho(k)$ [14], which we will henceforth call "Fourier space."

Fortunately, the machinery for inverting diffraction images of these types has already been well developed by Gerchberg, Fienup and others [14, 15]. Phase reconstruction or phase retrieval is a method for finding the real space signal generating a diffraction signal with a known modulus. The method operates via iterative projections onto supports in real space and Fourier space. The support in Fourier space is given by the diffraction data: Whatever the estimate of the real space image is, the magnitude of its Fourier transform must match what is seen on the detector. To perform this projection we use the magnitude projection operators given by

$$\tilde{P}_m(k) = \sqrt{I(k)}e^{i\varphi(k)} \quad (1.19)$$

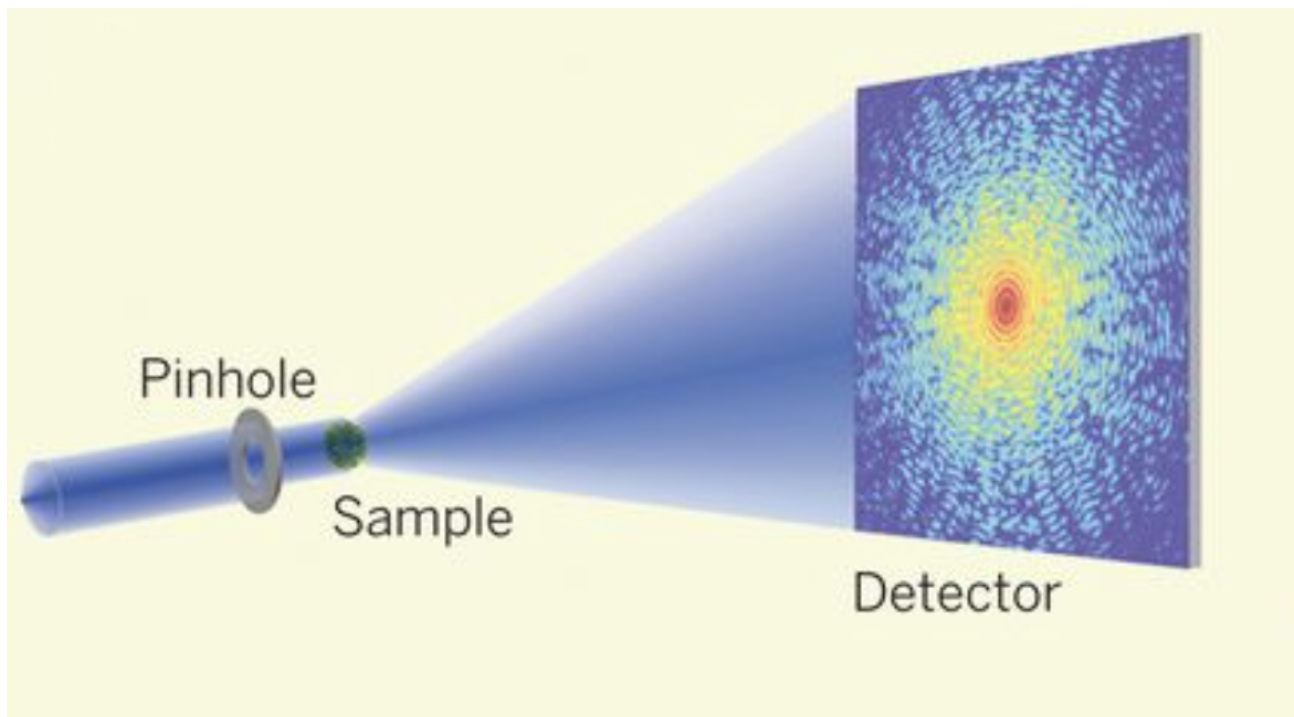


Figure 1.5: Diagram of coherent diffraction imaging experimental setup, (taken from the UCLA Coherent Imaging Group) [16]

$$P_m = \mathcal{F}^{-1} \tilde{P}_m \mathcal{F} \quad (1.20)$$

where $\rho(k)$ is the Fourier space estimate taken as the Fourier transform of the real space estimate $\rho(r)$, $\tilde{P}_m(k)$ is the magnitude projection operator in Fourier space, P_m is the magnitude projection operator in real space, $\varphi(k)$ is the phase of the Fourier space estimate, \mathcal{F} is the Fourier transform, and $I(k)$ is the known diffraction intensity. In effect, this operator simply attaches the correct magnitude to the far field phase generated by the real space object estimate.

The principle technique in phase reconstruction however is the real space constraint, often just referred to as the "Support." The real space support is a region in the real space image where the signal is allowed to be nonzero. The tighter the support is to the real space object, the smaller the space of possible configurations of the object, and thus a quality reconstruction is more likely to be found [17]. It should be noted that defining this support requires some apriori information about the object, which we will discuss later in this

thesis. Taking this support for granted we can define the following support projection operator:

$$P_s(r) = \begin{cases} \rho(r) & r \in S \\ 0 & r \notin S \end{cases} \quad (1.21)$$

where $P_s(r)$ is the support projection operator and S is the support region. In order to obtain a reconstruction of the image, the initial image is taken randomly, and we successively apply the supports to converge on an estimate of the real space object. This algorithm is sketched in Figure 1.6.

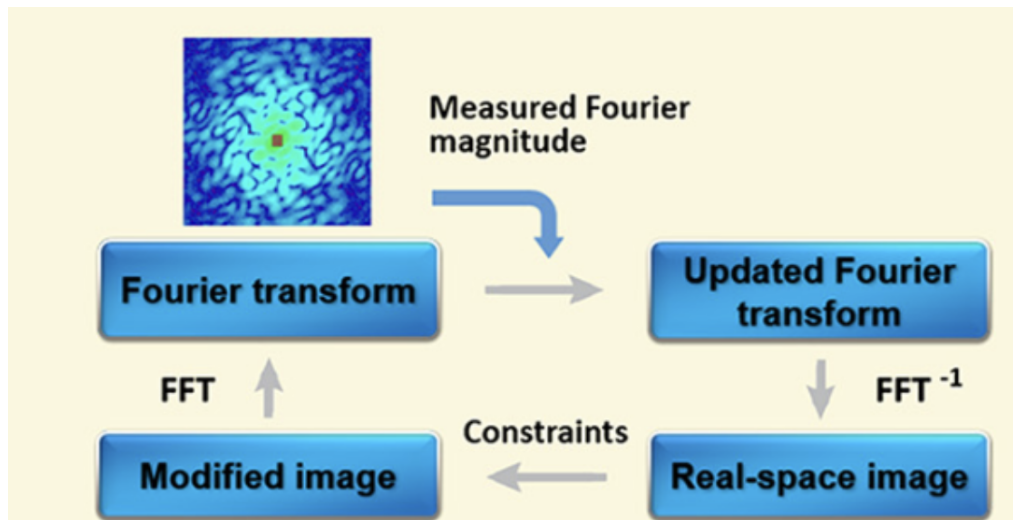


Figure 1.6: Diagram of phase reconstruction algorithm, (taken from the UCLA Coherent Imaging Group) [16]

CHAPTER 2

METHODS

2.1 Propagation of Radiation

The method for calculating the propagation of radiation results relatively directly from the simple forms in Equations (1.16) and (1.14). To do so we establish a three dimensional array indexed by polar angle θ , azimuthal angle ϕ , and frequency ω . We can then calculate the spectra produced at each detector point indexed by unique set of θ and ϕ values for each atom j in parallel. These spectra are then added to find the total macroscopic spectra. Here the linearity of electromagnetic radiation means that the entire propagation step can be calculated in parallel in whatever data structure for organizing the values (ω, θ, ϕ) is most computationally efficient since not only can the radiation for each atom be propagated in parallel, but it can be done for each component of the field E_ω . Furthermore each thread requires relatively little computing power since only one value, $a_j(\omega)e^{-i\frac{\omega}{c}r_j \cdot (\hat{r}_d - s\hat{L})}$, needs to be calculated on each thread. Therefore in general the propagation step can be easily scaled simply by employing more threads, even if used across multiple computing nodes. For 2D diffraction patterns this type of scalability was not necessary, instead all the propagation calculations in this thesis were performed on a single computing node with 24 threads. However increasing the number of atoms in the lattice, or the fidelity of the images would both likely require some more careful thought on how to best implement cross-node parallelization. We also note that all of these calculations were performed with a detector at some arbitrary distance from the sample, therefore the intensity values are also completely arbitrary. If one wishes to find some more physical values for the field, one could simply scale the arbitrary values calculated by the prefactor in Equation (1.13).

2.2 Diffractive Imaging

The most important aspect of further analysis of these diffractive images is to arrange them into a data structure that reduces the computational expense throughout the phase retrieval process. In phase retrieval the dominantly used operation will be Fourier and Inverse-Fourier transforms. The complexity of these operations can be vastly reduced by using the Fast Fourier Transform (FFT) algorithm. However this requires that the array being transformed is sampled on a regular interval. There are two possible ways to approach

this problem. Either this regular interval can be preselected in Cartesian coordinates, and then the corresponding set of θ and ϕ coordinates can be used during the propagation step. Alternatively, a regular grid of θ and ϕ can be used during the propagation step. In this case we can use Equations (1.18) and (1.17) to project onto Cartesian coordinates, and then interpolate the data onto a regular grid. The former offers some advantages when generating a large number of images since few steps are required to produce a Cartesian resolved image from the propagation step, while the latter offers some advantages in parallelization during the propagation step.

2.3 Phase Retrieval

Once a regularly-sampled Cartesian-resolved image is produced, we are ready to begin performing phase retrieval. The iterative projection algorithm described in section 1.2.3 was created by Gerchberg in 1972 [14]. Since then, significant improvements have been made to resolve some of the issues inherent in this algorithm, although iterative applications of support constraints remain core to almost all modern phase retrieval algorithms [15]. It was shown that Gerchberg’s algorithm was equivalent to gradient descent error reduction algorithms [15]. In the broader class of error reduction algorithms, the error is always reduced at each step. In some contexts this property is desirable since it is guaranteed that the algorithm will converge. However this convergence is **not** guaranteed to be on to the global minimum of error, equivalent to the true image. Instead the algorithm may converge on some local minima from which it cannot escape, leading to poor quality image reconstruction. Many modern phase reconstruction algorithms address this problem by incorporating a ”feedback” mechanism, introducing some instability, allowing the algorithm to escape these local minima. The work done in this thesis employs two of these feedback algorithms.

2.3.1 The Hybrid Input Output Method

The Hybrid Input Output algorithm (HIO) developed by Feinup [18] is the simplest implementation of this feedback mechanism, described below.

$$\rho_{(n+1)}(r) = \begin{cases} P_m \rho_{(n)}(r) & r \in S \\ [I - \beta P_m] \rho_{(n)}(r) & r \notin S \end{cases}, \quad (2.1)$$

where $\rho_n(r)$ is the real space estimate at the n th iteration, P_m is the magnitude projection operator given in Equation (1.20) and I is the identity operator and β is the feedback parameter. In the HIO algorithm instead of zeroing out everything outside of the real space support, we instead *reduce* the signal from the previous iteration outside of the support. Although the HIO algorithm is not guaranteed to converge since it does not monotonically decrease the error, the HIO algorithm has been shown to better reduce the error when it does converge as compared to the basic Gerchberg algorithm [17].

2.3.2 The Difference Map Method

In 2002 Elsner was able to incorporate a variety of phase retrieval methods in a single algorithm, the Difference Map [19]. The form of this algorithm is described below.

$$\rho_{(n+1)}(r) = I + P_s[(1 + \gamma_s)P_m - \gamma_s I] - P_m[(1 + \gamma_m)P_s - \gamma_m I]\rho_{(n)}(r), \quad (2.2)$$

where γ_m and γ_s are additional feedback parameters. In this thesis we take $\gamma_m = \frac{1}{\beta}$ and $\gamma_s = \frac{-1}{\beta}$. The analysis used to create this algorithm is beyond the scope of this thesis, however Elsner was able to show that with a positivity constraint ($\rho_n(r) > 0$) the difference map algorithm is especially effective at resolving structures of around 100 atoms. While the positivity constraint will not be satisfied since the microscopic spectra are complex valued, we will see later in this thesis that the algorithm remains effective.

We can see that the difference map algorithm employs many more operations and thus is more expensive than the HIO algorithm, however as previously discussed, it has some properties that makes it better suited for reconstructing the image of a sparse arrangement of atoms. Depending on how the algorithm is implemented it may be more advantageous to employ a Difference Map algorithm which may take fewer more expensive iterations, or an HIO algorithm which takes a larger number of cheaper iterations.

In practice, whether using HIO or DM, a small number of iterations of error reduction steps are used every ten to twenty iterations of HIO/DM since this tends to give better convergence properties of "exploring" local minima ensuring the algorithm does at least begin to descend into these saddle points [17]. Furthermore, a larger number of error reduction iterations are often used at the very end of the algorithm to ensure the solution has fully descended into the nearest local minimum in the error landscape.

2.3.3 Optical Lattice Supports

The last step remaining before we can perform phase reconstruction is to set a real space support for the optical lattice. Although we may not know where the atoms in the lattice are, we do know that the optical lattice will bind whatever atoms are present into the lattice site. Therefore a good potential estimate for the real space support would be a tight region around each lattice site, which should be relatively precisely known to the experimentalists. This type of support is shown in Figure 2.1.

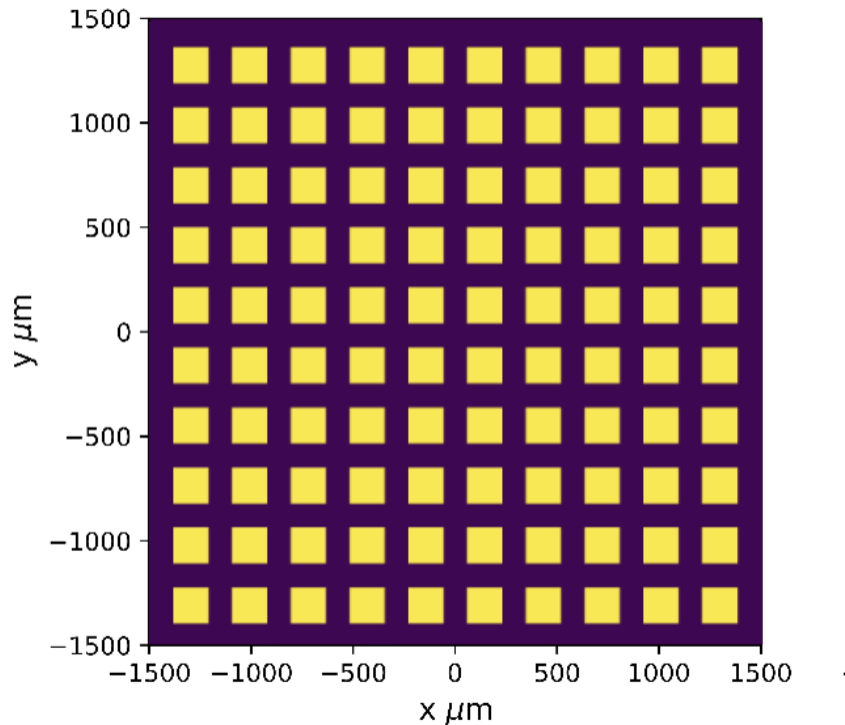


Figure 2.1: Real space support for phase reconstruction in an optical lattice.

We note that the region of support around each lattice site can be adjusted based on the wavelength being used for the reconstruction. The size of the image of each atom can be estimated by using the inverse Fourier transform of Equation (1.13), and the region of support can be taken to be around this size. This means that the support around each site can be reduced when using images generated from higher harmonics.

CHAPTER 3

RESULTS WITH STATIC SUPPORT

Using the method described in the previous Chapter, we have solved the TDSE for a set of 100 hydrogen atoms in an optical lattice with 300 nm interatomic spacing interacting with the field of a 20 cycle pulse with a sine-squared envelope at a wavelength of 800 nm, having a $30\mu\text{m}$ beam waist and a peak intensity of 10^{14} W/cm^2 . The laser was centered at the center of the optical lattice, and the lattice plane was placed at the beam focus. Therefore, the peak intensity for each atom in the lattice was calculated using

$$I_r = I_0 \exp\left(\frac{-2r^2}{w_0^2}\right) \quad (3.1)$$

where I_0 is the peak intensity for the beam, r is the radial distance from the center of the focus, and w_0 is the beam waist. In the present study the field at each atom was taken to be the same field as the beam center, i.e. $I_r = I_0$. Since the beam waist is large compared to the interatomic spacing, we also approximated the variation in carrier envelope phase to be negligible. These microscopic spectra were then propagated into the far field and projected onto a regular Cartesian diffraction pattern via 2D interpolation across the irregular diffraction image. We then performed phase reconstruction using the Difference Map method using $\beta = 0.7$, with one iteration of error reduction every 10 iterations of Difference Map iterations, and 100 error reduction iterations at the end of reconstruction. An example can be seen in Figure 3.1.

Here three regimes were specified: the highly filled regime where most of the lattice sites are filled (90-100 filled sites); the half filled regime where around half of the sites are filled (45-55 filled sites), and the sparsely filled regime (0-10 filled sites). For a specific reconstruction the number of filled sites in each one of these regimes was chosen at random.

We see that in general the phase reconstruction will produce poor quality reconstructions in the highly filled and sparsely filled regime, while the half-filled regime produces relatively accurate reconstructions. In the highly filled regime this is likely because the object being reconstructed is still highly regular, which will result in a very strong diffraction pattern. This means that the lower order features resulting from only a few missing lattice sites will be more difficult to resolve, and the reconstruction will likely converge on an image with all the lattice sites filled. Indeed, this is what we see in the bottom left of Figure 3.1. Interestingly, this

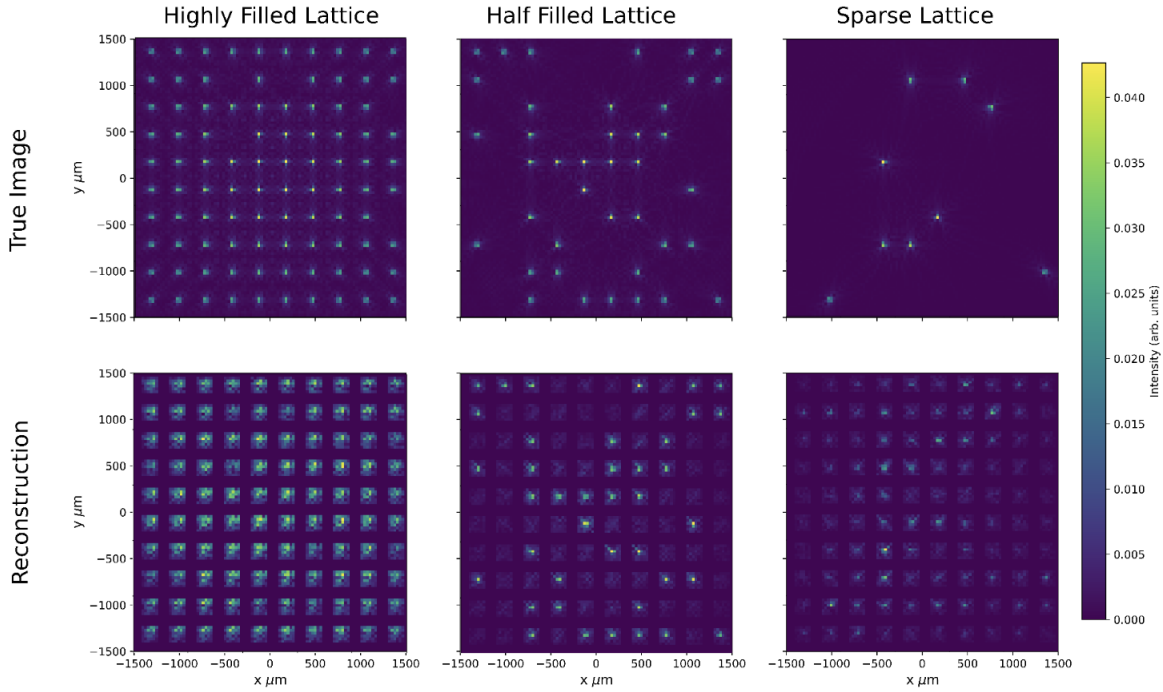


Figure 3.1: Reconstructed images for optical lattices with different number of lattice sites filled using the image generated by the seventh harmonic. From left to right; 96 filled sites, 47 filled sites, 9 filled sites

does mean that this type of static support for phase reconstruction discussed in section 2.3.3 will perform very well if every lattice site is filled, since the only features present will be these strong high order features produced by the completely regular object as can be seen in Figures 3.2 for a 1D regularly filled lattice and 3.3 for a 2D regularly filled lattice.

In fact, the Figures above were taken with an even looser support of a square region encompassing the entire lattice. Even under this loose support, the strong diffraction magnitudes from the regularity of the lattice forces the algorithm into the correct solution in very small number of iterations (less than 100). This again shows that in the highly filled regime the algorithm will tend towards a reconstruction with all the lattice sites filled. We note that the data in Figure 3.3 also show the behavior of the Difference Map algorithm in avoiding local error minima, at around iteration step 20.

Conversely, for the sparsely filled regime, there will be many empty lattice sites. This means that most of the support will be empty, and thus the support will be very loose. Essentially, we will encounter the same issue that phase reconstruction attempts to address, there are many possible configurations of the lattice, even within the support, that may produce the diffraction data seen, and the algorithm is likely not to converge to

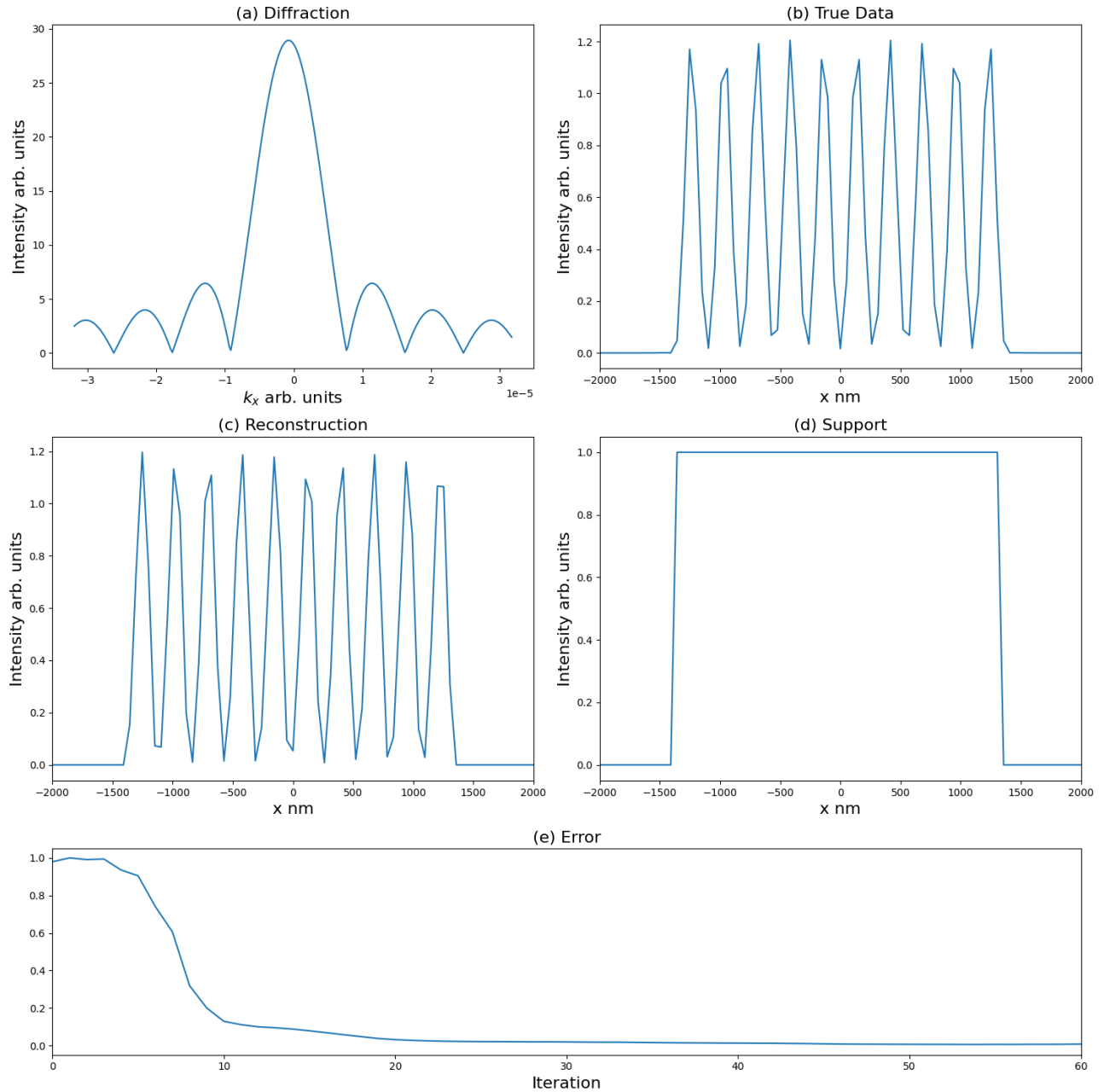


Figure 3.2: Phase reconstruction of a 1D lattice of 10 hydrogen atoms using the 7th harmonic and a Difference Map method with static support. Shown are the diffraction data (a), the magnitudes of the true real space data taken as the inverse Fourier transform of the diffraction data with phase (b), final reconstruction (c) and static support of a bounding box around the optical lattice (d), and the error over iterations (e)

the true image.

For the half filled regime, there is just enough missing lattice sites to break up the regularity in the object, but not so many that the support becomes too loose to be effective. In this case we generally see good quality reconstructions.

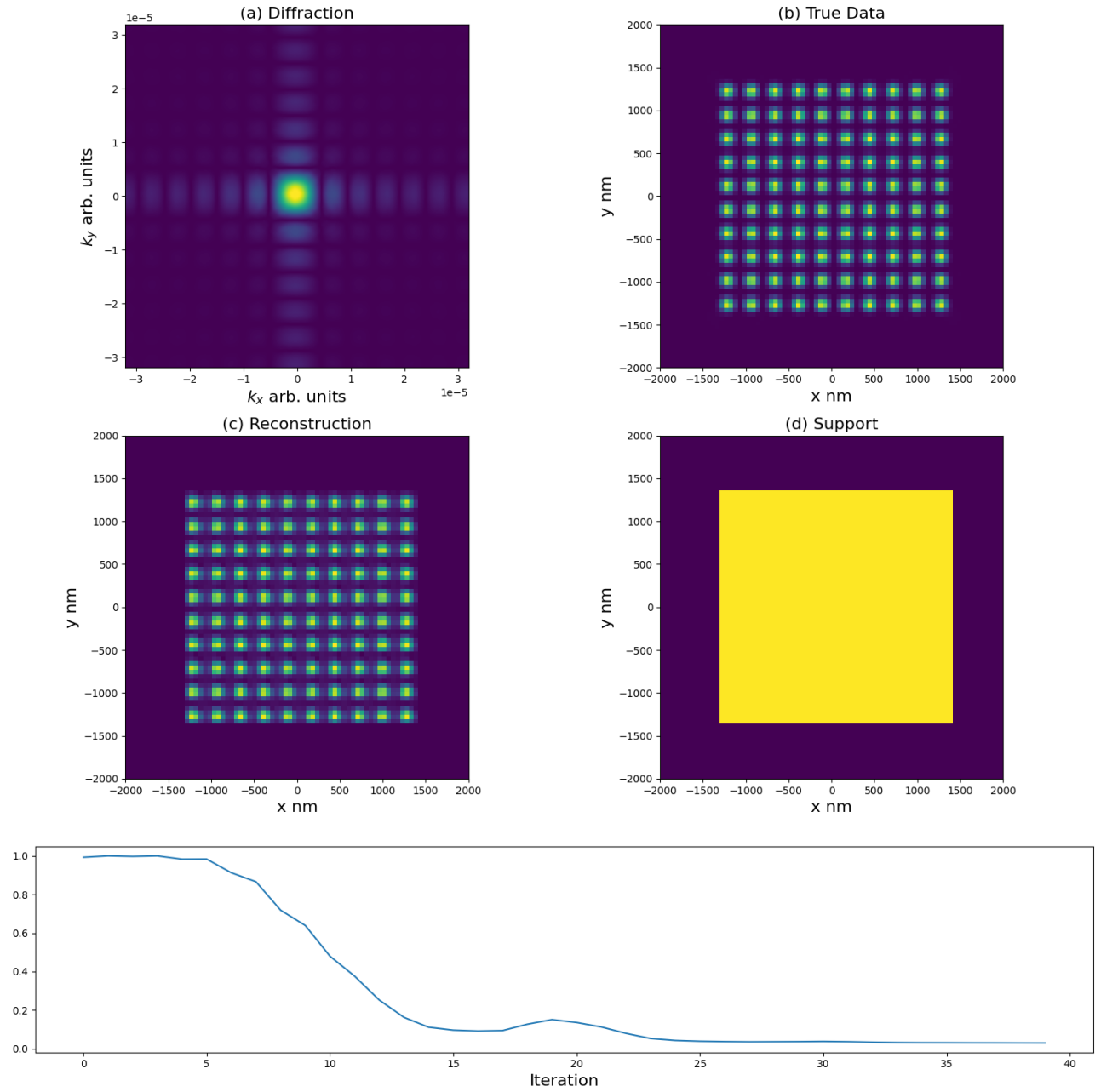


Figure 3.3: Same as Figure 3.2 but for a 2D lattice of 10×10 hydrogen atoms.

Thus, we see that the support is largest determining factor in the quality of a reconstruction [20]. Our initial strategy of determining a static support using only information about the lattice sites is thus not an effective strategy for performing phase reconstruction.

CHAPTER 4

DYNAMIC SUPPORT

We now address the issue of determining better real space supports for the phase reconstruction process. One potential strategy could be to use results from other techniques such as fluorescence imaging of the lattice, to determine which sites are occupied, use this to determine a support only around each one of those sites, and then performing HHG diffractive imaging with phase reconstruction to develop a much higher definition image. However, the topic of fluorescence imaging is outside the scope of this thesis, and we instead focus on generating high definition images with as little a-priori information about the sample as possible.

To do this we wish to find a method for adjusting the support to each one of these regimes in order to more consistently generate high quality reconstruction. Again, fortunately some techniques in this regard have already been developed to address similar support issues in other areas of coherent diffractive imaging.

4.1 Shrink Wrapping: Concept and Implementation

Shrink wrapping is a method for dynamically adjusting the support throughout the reconstruction process so that a support can be determined without a-priori information about the sample aside from its diffraction magnitudes [21]. The technique works as follows:

1. Blur the current real space estimate of the object.
2. Take the new support to be the pixels above some intensity cutoff.
3. Continue reconstruction with the new support.

In this way, each time shrink wrapping is applied the support should "shrink" around the real space object as it is exemplified in Figure 4.1.

To blur the real space image we apply a Gaussian filter to our image which can be defined as follows:

$$g(r) = \exp\left(-\frac{r^2}{2\sigma^2}\right), \quad (4.1)$$

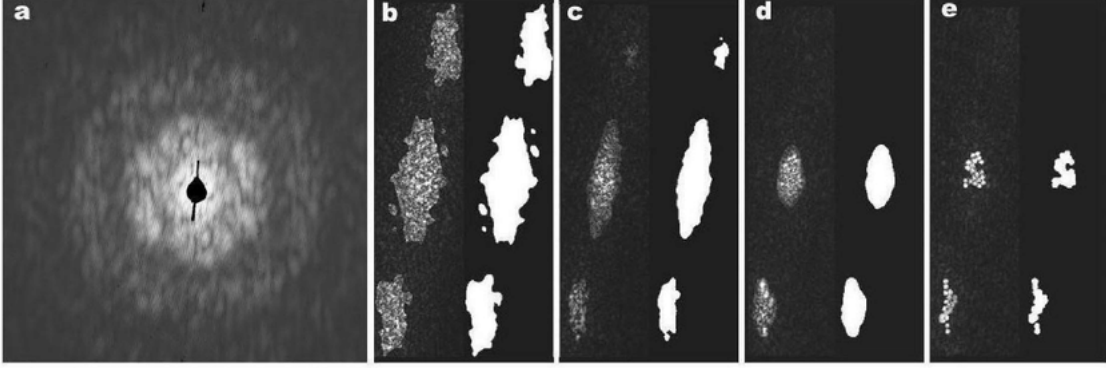


Figure 4.1: Phase reconstruction of gold pellets with shrink wrapping. (a) The diffraction pattern of the object. (b,c,d) Evolution of reconstruction and support with shrink wrapping with the left inset being the reconstruction at the iteration and the right inset being the support. The quality of the reconstruction increases substantially as the support grows tighter to the gold pellets seen in (d) (taken from Marchesini et al. [21]).

where $g(r)$ is a Gaussian with σ being the standard deviation or "width". Then to blur the image with this filter we use

$$\rho_{\text{blur}}(r) = (\rho * g)(r) = \mathcal{F}^{-1}(\mathcal{F}(\rho(r))\mathcal{F}(g(r))). \quad (4.2)$$

More simply put, we convolute the Gaussian with the current estimate, where σ is a parameter that characterizes how much the image is blurred. In order to produce the new support we apply

$$s_{\text{shrink}}(r) = \begin{cases} 1 & \frac{|\rho_{\text{blur}}(r)|}{\max|\rho_{\text{blur}}|} \leq c \\ 0 & \frac{|\rho_{\text{blur}}(r)|}{\max|\rho_{\text{blur}}|} > c \end{cases}, \quad (4.3)$$

where c is the intensity cutoff taken as some fraction of the maximum intensity of the blurred real space estimate.

We note with $\sigma \rightarrow 0$, $g(r)$ will begin to approach a delta function in which case $\rho_{\text{blur}}(r) = \rho(r)$. In this case the shrink wrapping step will adjust the support to be the pixels below some intensity cutoff of the current image without blurring. We can see that this may be problematic since if we were to reach a true reconstruction of the image, we would begin removing pixel below this cutoff and subsequently converge on an incorrect reconstruction. Therefore, if σ is taken too small we are likely not get good convergence behavior. Conversely, if the blurring is taken to be too large, then the entire image will have about the same intensity and none of the object structure will be seen in the shrink wrapping step. Determining the σ range in which we get good shrink behaviour will thus depend somewhat on the object being reconstructed itself.

We also note that there must be some spacing between shrinking wrapping iterations in order to get good convergence properties. This is because if shrink wrapping is performed at each step the algorithm will have little time to approach the closest local minimum before the support is changed, likely displacing the estimate from this minimum. Conversely, if shrink wrapping is performed too infrequently, then we lose the benefits of dynamic support updating. In general, a good frequency of shrink wrapping iterations will be around every 10-100 iterations [21].

4.2 Results with Shrink Wrapping

We applied Shrink Wrapping using a Difference map method with a Gaussian filter of 2 pixels width with Shrink Wrapping performed every 100 iterations of Difference Map iterations for both 2D and 1D lattices which are shown in the Figures below.

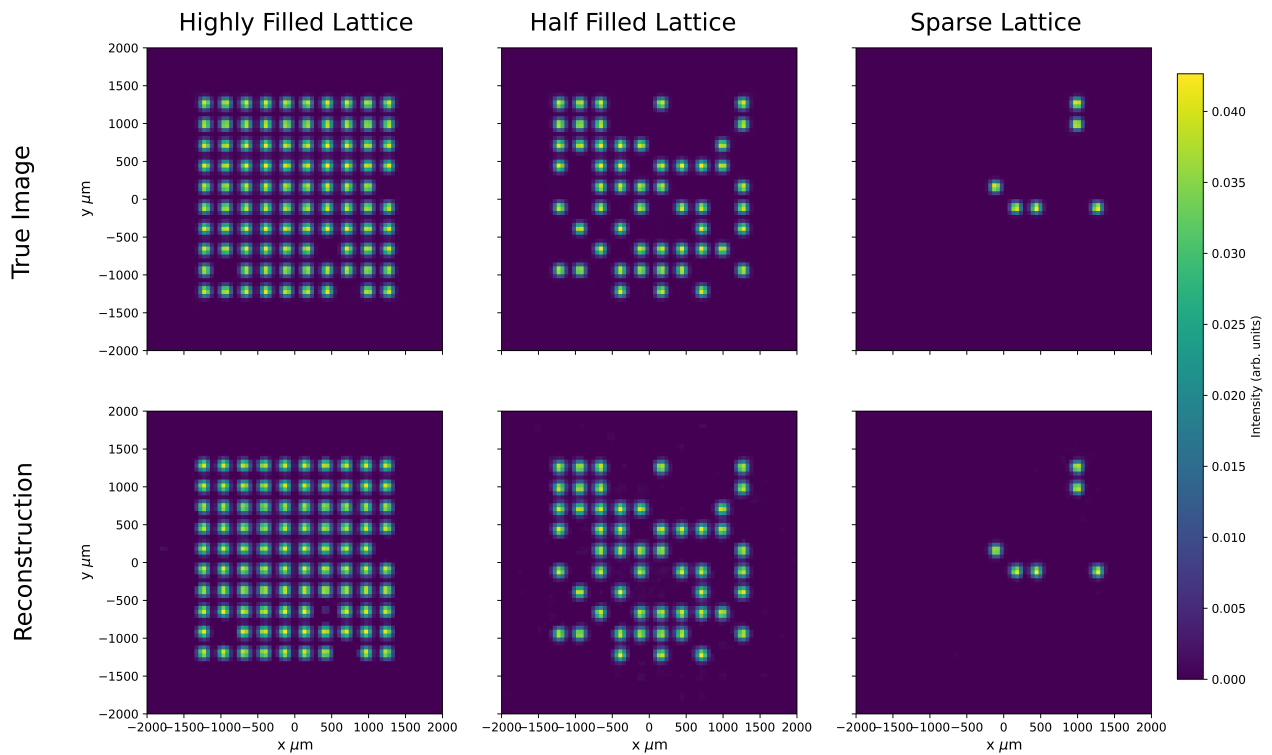


Figure 4.2: Reconstructions of a 10×10 lattice of hydrogen atoms in three different regimes with 300 nm interatomic spacing using the seventh harmonic with a Difference Map method and Shrink Wrapping.

We first note that using this technique we were able to generate near perfect reconstructions up to trans-

lation, reflection, and a global phase factor, which are considered to be equivalent images. This technique was successful in all three regimes described previously as can be seen in Figure 4.2.

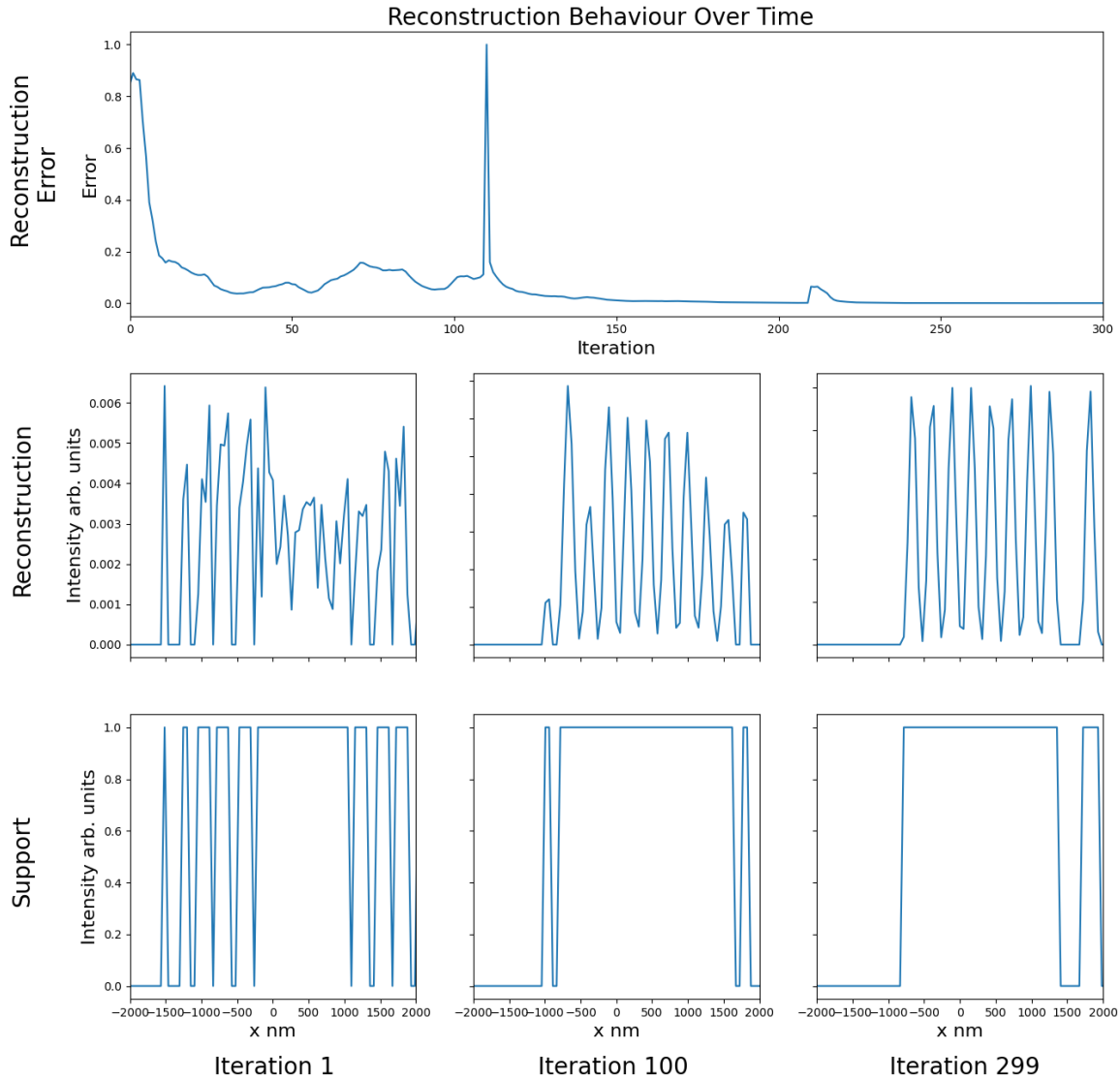


Figure 4.3: Reconstruction behaviour over time for a 1D lattice of 9 hydrogen atoms using the seventh harmonic and a Difference Map method with Shrink Wrapping including the error over time (top row), reconstruction over time (middle row), and support over time (bottom row)

The reconstruction behaviour for both 1D and 2D lattices are shown in Figures 4.3 and 4.4 where the evolution of the support and corresponding reduction in error of the reconstruction are shown. One can see

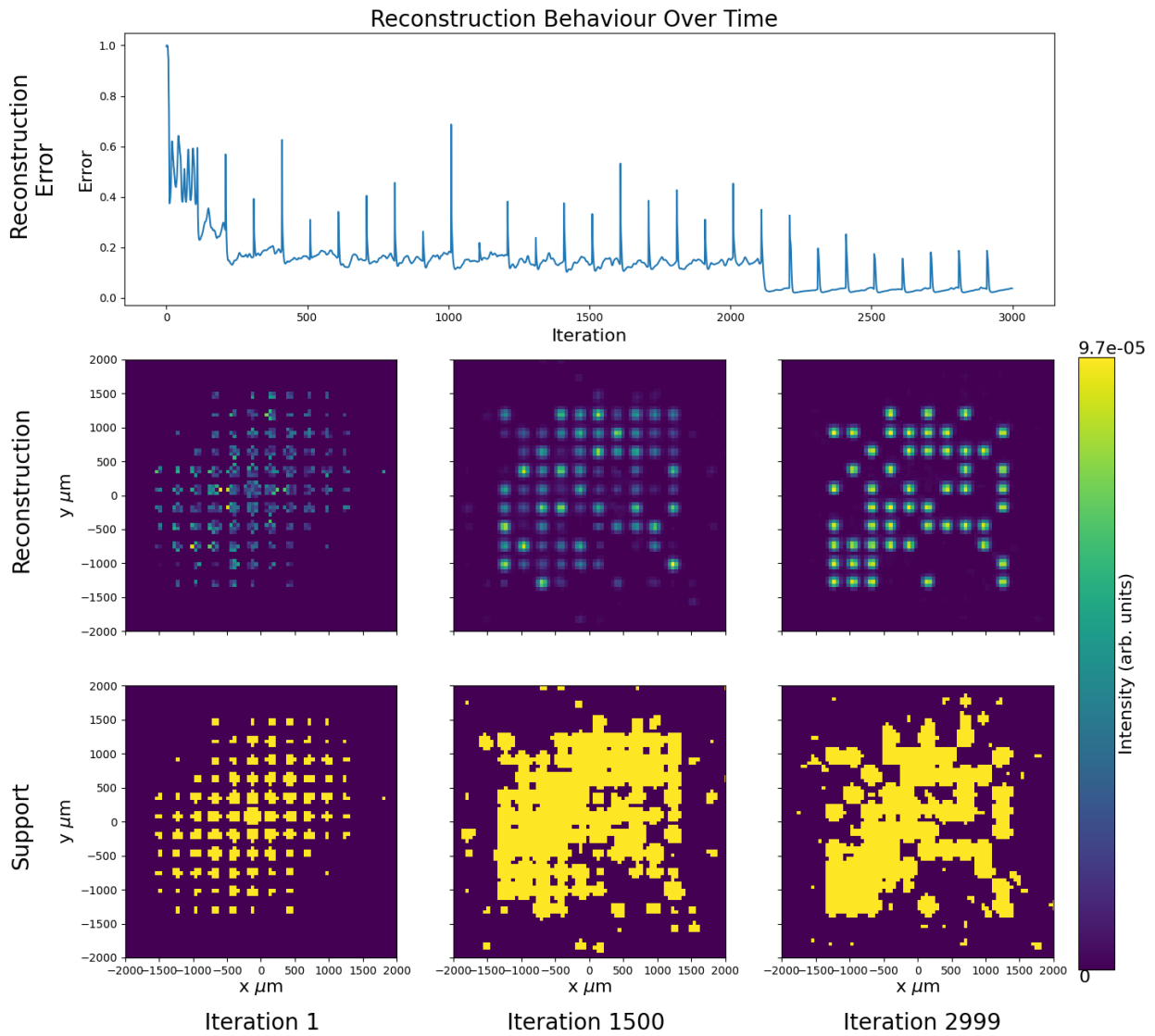


Figure 4.4: Same as Figure 4.3 for a 2D lattice of 53 hydrogen atoms.

large spikes in the error which correspond to these Shrink Wrapping steps, which are followed by steep reductions in error. This type of behaviour again shows how the quality of support can drastically change the convergence properties of the reconstruction. For the 1D case in Figure 4.3 one atom was removed to ensure the algorithm could resolve lower order features even in highly regular objects, the success of which can be seen in Figure 4.5

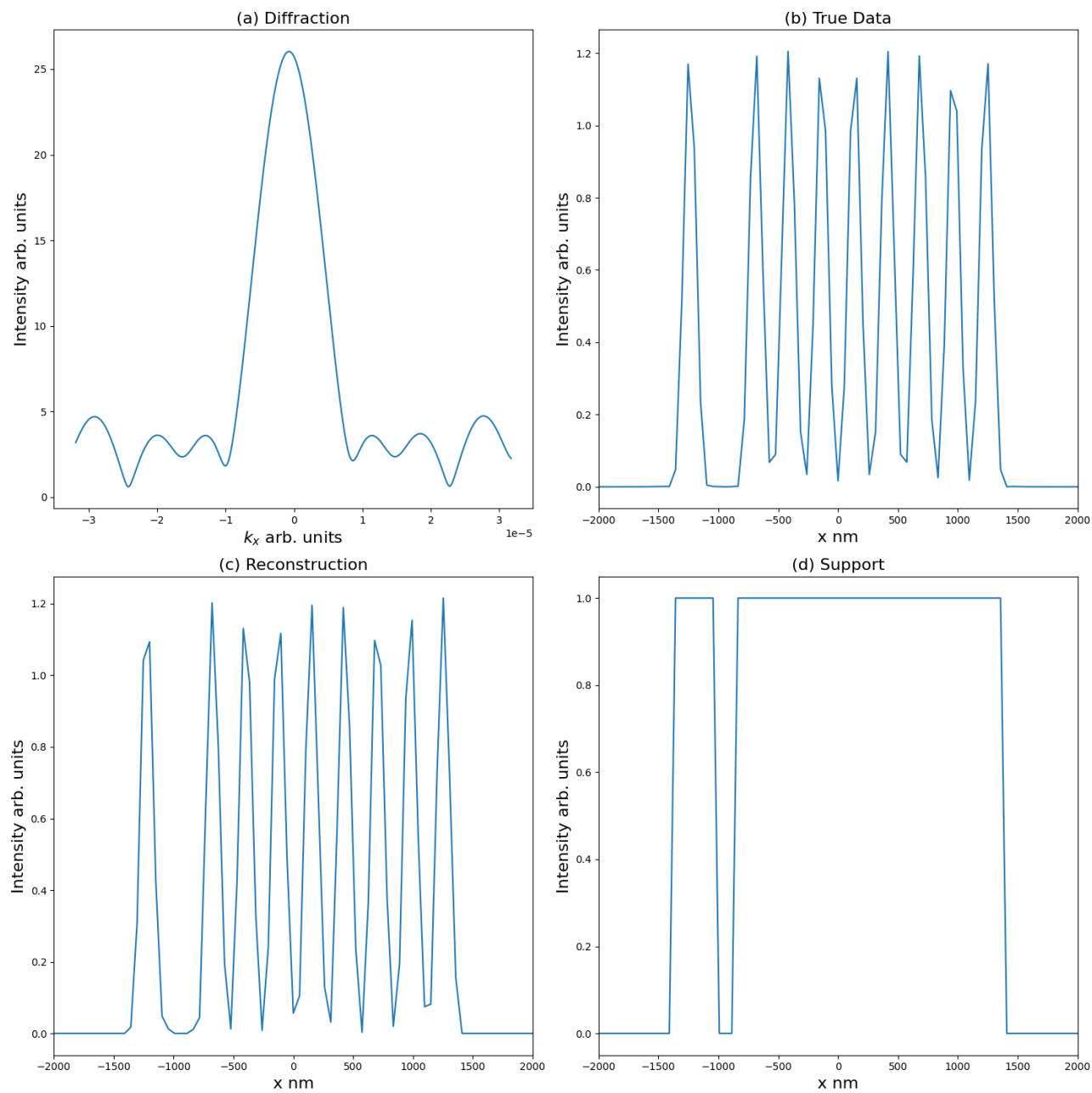


Figure 4.5: Phase reconstruction of 1D lattice with one empty site.

The number of iterations to reach convergence was significantly higher in the 2D case than in the 1D case, which is expected since in the 2D reconstruction we must resolve N^2 pixels as compared to the N pixels of the 1D case at the same resolution. Furthermore, a Gaussian filter with a width of 2 pixels was applied in both the 1D and 2D cases which agrees with findings by Marchesini et al. [17]. For the 1D case a Shrink Wrapping threshold of $c = 0.4$ was used, while in the 2D case $c = 0.2$ was used. These values were determined by scanning the quality of reconstructions over the two dimensional parameter space of Gaussian filter width and Shrink Wrapping threshold.

CHAPTER 5

OUTLOOK

5.1 3D Imaging

While this thesis only explored 2D images of lattices, in principle all of the techniques can be extended to imaging of 3D lattices. To do this, one must generate a diffraction volume of the sample rather than a diffraction image. Importantly, this can be done using a nearly identical experimental setup to the one used in 2D imaging. However, the object of interest must be rotated in order to gain the necessary information to perform this type of imaging. The technique works by stitching together 2D diffraction planes at a range of angles into a diffraction volume [22] as can be seen in Figure 5.1.

5.1.1 Diffraction Volumes

To perform such calculations we would pick a set of diffraction planes which will form the diffraction volume. The volume can then be defined uniquely as the tangent space to the unit sphere for some angles θ_{plane} and ϕ_{plane} . One then either rotates the sample into this plane or the laser propagation direction normal to the plane accordingly. The diffraction image can be calculated exactly as before. Each point in the diffraction image can be matched with a point on the diffraction sphere using the equations below. Without loss of generality the laser propagation direction is picked to be in the \hat{z} -direction and the rotation direction has been chosen to be around the x -axis. In this case the coordinate transformations are relatively simple.

$$\begin{aligned} E_{x'} &= E_x \cos(\theta) \\ E_{y'} &= E_y, \\ E_{z'} &= E_z \sin(\theta) \end{aligned} \tag{5.1}$$

where the unprimed coordinates are the coordinates taken from each 2D diffraction image as before, the primed coordinates are the coordinates of the diffraction volume, and θ is the degree of rotation around the x -axis.

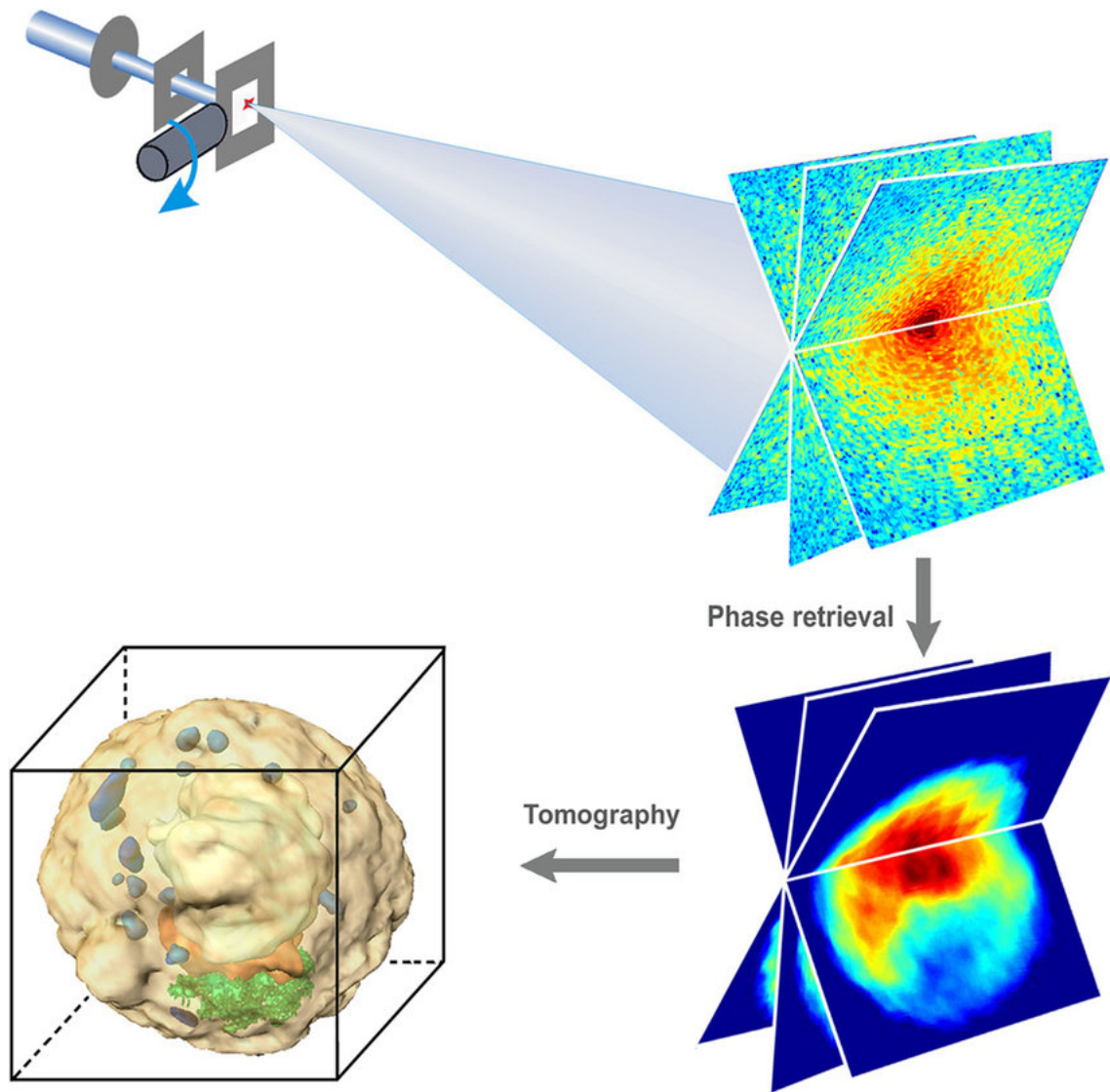


Figure 5.1: Schematic layout of 3D X-ray diffraction (taken from H. Jiang et al. [22]).

We also note that for the 3D lattice one must now consider the field distribution of the laser in 3D, i.e.

$$\begin{aligned}
 I(r, z, \omega) &= I_0 \left(\frac{w_0}{w(z)} \right)^2 \exp \left(\frac{-2r^2}{w(z)^2} \right) \\
 w(z) &= w_0 \sqrt{1 + \left(\frac{z}{z_R} \right)^2}, \\
 z_R &= \frac{\pi w_0^2 n}{\lambda}
 \end{aligned}
 \tag{5.2}$$

where z is the distance from the focus along the beam and z_R is the Rayleigh range.

5.1.2 Computational Considerations

Generating these 3D diffraction volumes inherently carries some computational hurdles not present with 2D diffraction images. First, new microscopic spectra must be calculated for each atom in the lattice for every 2D snapshot since the laser field including polarization direction and spatial profile will change as the beam is rotated relative to the sample. Furthermore, if one wish to maintain the same resolution in these 3D diffraction volumes as for the 2D diffraction images then the number of snapshots must be similar to the number of desired pixels in each 2D slice of the diffraction volume.

This introduces compounding computational complexity. First, the microscopic spectra must be recalculated for every snapshot, and the spectra must also be propagated into the far field for each snapshot. This can be an issue since even a relatively coarse resolution such as 300×300 pixels would mean that calculating a 3D volume of $300 \times 300 \times 300$ pixels, which will be 300 times as computationally expensive. With a $10 \times 10 \times 10$ lattice of atoms this quickly becomes increasingly difficult to calculate directly, since it requires 3000 times as many computations as the 2D image of the 10×10 lattice. Therefore, we must find a way to reduce the computational complexity of this process. We note that the propagation step is much faster than the TDSE step and can be more easily parallelized as discussed previously. Because of this we focus on how to speed up the computations of the TDSE step needed for finding the microscopic spectra. In the next subsection we outline an alternative (approximative) method to the computationally intensive TDSE calculations.

5.2 Strong Field Approximation

An alternative to the TDSE is called the "Strong Field Approximation (SFA)" or "Semiclassical Approximation." The SFA seeks to decrease the complexity of finding the dipole of the electron wave function $\vec{D}(t) = \langle \Psi(\vec{r}, t) | \vec{d} | \Psi(\vec{r}, t) \rangle$ as compared to a fully quantum-mechanical TDSE calculation by reducing the problem to the semiclassical model discussed in the text along with Figure 1.3. To reiterate, this model includes 3 steps:

1. Tunnel Ionization into the continuum.
2. "Classical" propagation of the electron in continuum subject only to the laser field.
3. Recombination and photoemission of the electron with its parent nucleus.

We represent this process via the following integral expression [23]

$$\vec{D}(t) = i \int_t^{t_0} dt' \int d\mathbf{p} \mathbf{d}^*(\mathbf{p} + \mathbf{A}(t)) e^{-iS(\mathbf{p}, t, t')} \mathbf{E}(t') \mathbf{d}(\mathbf{p} + \mathbf{A}(t')), \quad (5.3)$$

where t_0 is the ionization time of the electron, t is the recombination time, \mathbf{p} is the momentum of the electron, \mathbf{E} is the electric field, \mathbf{A} is the vector potential, $S(\mathbf{p}, t, t')$ is the action of the electron, and $\mathbf{d}(\mathbf{p} + \mathbf{A}(t))$ is the dipole transition matrix element from the ground state to a continuum state with momentum $\mathbf{p} + \mathbf{A}(t)$. The classical action is the kinetic energy minus the potential energy of the electron which can be written as

$$S(\mathbf{p}, t, t') = \frac{1}{2} \int_{t'}^t [\mathbf{p} + \mathbf{A}(\tau)]^2 d\tau + I_p(t - t'), \quad (5.4)$$

This is directly equivalent to the classical action picked up by a charged particle with initial momentum \mathbf{p} under the effects of a vector potential \mathbf{A} from time t to t' . The dipole transition element is defined as

$$\mathbf{d}(\mathbf{p} + \mathbf{A}(t)) = \langle \mathbf{p} + \mathbf{A}(t) | \hat{\mathbf{d}} | g \rangle, \quad (5.5)$$

where $\langle \mathbf{p} + \mathbf{A}(t) |$ is the continuum state, $\hat{\mathbf{d}}$ is the dipole operator and $|g\rangle$ is the ground state. For the hydrogen atom an exact analytic form for these transition elements can be found, however for other species these matrix elements will need to be calculated numerically. Fortunately, these elements can be precomputed since they depend only on the ionic potential and not on the laser parameters, and therefore make negligible

contributions to the computational cost.

The expression for the SFA in Equation (5.3) essentially states to sum over all the ways the electron can **ionize**, **propagate**, and **recombine** while attaching the correct **phase** to each one of these processes. Although this may seem rather ad hoc, this form for the dipole $D(t)$ can be explicitly derived from splitting the full electron wave function into a non-interacting component and interacting component. One can then make the approximation that during the propagation of the electron in the strong field, the ionic potential should be negligible to the laser potential and can be disregarded in the interacting component [23].

While this approximation massively reduces the complexity of calculating the dipole as compared to the full TDSE since we do not need to calculate a full wave function at each time step, it is still rather expensive since we must integrate over all momenta and ionization times for each time step.

5.2.1 The Stationary Phase Approximation

We can further reduce the complexity of the calculation by noting that the action in Equation (5.4) will in general vary rapidly with respect to the momentum \mathbf{p} . This means integrating over the momenta the phases associated with the action will tend to cancel out except when the action varies slowly with respect to \mathbf{p} . It can be proven rigorously in these situations, using what is called **stationary phase** or saddle point approximation, that the dominant contributions to the momentum integral will arise only when the rate of change of the phase is zero, i.e. for the saddle points of the action with respect to \mathbf{p} [23].

Therefore, we can reduce the momentum integral to just a single momentum at each point where the action is minimized.

$$\begin{aligned}
 \frac{\partial S}{\partial \mathbf{p}} &= 0 \\
 &= \frac{\partial}{\partial \mathbf{p}} \left[\frac{1}{2} \int_{t'}^t [p^2 + 2\mathbf{p} \cdot \mathbf{A}(\tau) + A(\tau)^2] d\tau + I_p(t - t') \right]. \\
 &= (t - t')\mathbf{p} + \int_{t'}^t \mathbf{A}(\tau) d\tau
 \end{aligned} \tag{5.6}$$

Solving for \mathbf{p} we find the saddle point momentum p_s to be

$$p_s(t, t') = -\frac{1}{t - t'} \int_{t'}^t \mathbf{A}(\tau) d\tau. \tag{5.7}$$

The form for the dipole in Equation (5.3) then becomes

$$\vec{D}(t) = i \int_t^{t_0} dt' \mathbf{d}^*(\mathbf{p}_s(\mathbf{t}, \mathbf{t}') + \mathbf{A}(t)) e^{-iS_s(t, t')} \mathbf{E}(t') \mathbf{d}(\mathbf{p}_s(\mathbf{t}, \mathbf{t}') + \mathbf{A}(t')). \quad (5.8)$$

We note that if the dipole time step Δt is taken to be the same as the integral time step $\Delta t'$, then one can essentially precompute the saddle point momenta $p_s(t, t')$ by precomputing some array $\mathcal{A}(t) = \int_0^t A(\tau) d\tau$ since there will be a large amount of redundancy from the time integral of the vector field in calculating the saddle point momentum for each combination of ionization and recombination times. However, there is more work to be done to show if using this time step reduction is a numerically stable and effective way of employing the saddle point approximation. A potential source of error could be that $D(t)$ at small t will be calculated over relatively few integration steps, while at large t steps it will be calculated over many integration steps, and thus may be better converged.

Regardless, this method offers some unique advantages in that it can be used with any well defined vector potential, regardless of beam shape or laser parameters, which may make it better suited for extending these type of calculations for exploring imaging methods such as Ptychography [24]. However, the SFA has been shown to poorly agree with full TDSE calculations at the lowest harmonics, and thus may only be suited for high frequency imaging calculations. We also note that these SFA calculations are well suited for other areas of macroscopic HHG research including those with more complex fields such as cross-polarized setups or elliptically polarized laser where large number of TDSE calculations can become intractable.

REFERENCES

- [1] R. Hooke, J. Allestry, and J. Martyn, *Micrographia, or, Some physiological descriptions of minute bodies made by magnifying glasses :with observations and inquiries thereupon*. London, Printed by Jo. Martyn and Ja. Allestry, printers to the Royal Society, 1665, 1665, p. 323, <https://www.biodiversitylibrary.org/biblio>
- [2] H. Geiger and E. Rutherford, “On the scattering of the α -particles by matter,” *Proceedings of the Royal Society of London. Series A, Containing Papers of a Mathematical and Physical Character*, vol. 81, no. 546, pp. 174–177, 1908. eprint: <https://royalsocietypublishing.org/doi/pdf/10.1098/rspa.1908.0067>.
- [3] G. Aad *et al.*, “Observation of a new particle in the search for the Standard Model Higgs boson with the ATLAS detector at the LHC,” *Phys. Lett. B*, vol. 716, pp. 1–29, 2012. arXiv: 1207.7214 [hep-ex].
- [4] E. Abbe, “Beiträge zur theorie des mikroskops und der mikroskopischen wahrnehmung,” *Archiv für mikroskopische Anatomie*, vol. 9, pp. 413–418, 1873.
- [5] C. Bevis, “Ptychography coherent diffractive imaging systems for extreme ultraviolet and x-ray sources,” Ph.D. dissertation, Boulder, 2020-11 2020, p. 129.
- [6] D. F. Gardner *et al.*, “Subwavelength coherent imaging of periodic samples using a 13.50.25emnm tabletop high-harmonic light source,” *Nature Photonics*, vol. 11, no. 4, pp. 259–263, Mar. 2017.
- [7] M. Born and R. Oppenheimer, “Zur quantentheorie der molekeln,” *Annalen der Physik*, vol. 389, no. 20, pp. 457–484, 1927. eprint: <https://onlinelibrary.wiley.com/doi/pdf/10.1002/andp.19273892002>.
- [8] M. Awasthi, Y. V. Vanne, A. Saenz, A. Castro, and P. Decleva, “Single-active-electron approximation for describing molecules in ultrashort laser pulses and its application to molecular hydrogen,” *Phys. Rev. A*, vol. 77, p. 063 403, 6 Jun. 2008.
- [9] J. P. Edwards, U. Gerber, C. Schubert, M. A. Trejo, and A. Weber, “The Yukawa potential: ground state energy and critical screening,” *Progress of Theoretical and Experimental Physics*, vol. 2017, no. 8, 083A01, Aug. 2017.
- [10] T. Popmintchev *et al.*, “Bright coherent ultrahigh harmonics in the kev x-ray regime from mid-infrared femtosecond lasers,” *Science (New York, N.Y.)*, vol. 336, pp. 1287–91, Jun. 2012.
- [11] M. F. Parsons *et al.*, “Site-resolved imaging of fermionic ${}^6\text{Li}$ in an optical lattice,” *Phys. Rev. Lett.*, vol. 114, p. 213 002, 21 May 2015.
- [12] R. Reiff, “Atomic characteristics and high-order harmonic spectra: Extension of ab-initio numerical calculations to larger systems,” Ph.D. dissertation, Boulder, May 2021.

- [13] C. Hernández-García, J. A. Pérez-Hernández, J. Ramos, E. C. Jarque, L. Roso, and L. Plaja, “High-order harmonic propagation in gases within the discrete dipole approximation,” *Phys. Rev. A*, vol. 82, p. 033432, 3 Sep. 2010.
- [14] R. W. Gerchberg, “A practical algorithm for the determination of phase from image and diffraction plane pictures,” *Optik*, vol. 35, pp. 237–246, 1972.
- [15] J. Fienup, “Phase retrieval algorithms: A comparison,” *Applied optics*, vol. 21, pp. 2758–69, Aug. 1982.
- [16] U. C. I. Group. “Coherent diffractive imaging (cdi).” ().
- [17] S. Marchesini, “Invited article: A unified evaluation of iterative projection algorithms for phase retrieval,” *Review of Scientific Instruments*, vol. 78, pp. 011301–011301, Feb. 2007.
- [18] J. R. Fienup, “Reconstruction of an object from the modulus of its fourier transform,” *Opt. Lett.*, vol. 3, no. 1, pp. 27–29, Jul. 1978.
- [19] V. Elser, “Phase retrieval by iterated projections,” *J. Opt. Soc. Am. A*, vol. 20, no. 1, pp. 40–55, Jan. 2003.
- [20] J. R. Fienup, “Reconstruction of a complex-valued object from the modulus of its fourier transform using a support constraint,” *J. Opt. Soc. Am. A*, vol. 4, no. 1, pp. 118–123, Jan. 1987.
- [21] S. Marchesini *et al.*, “X-ray image reconstruction from a diffraction pattern alone,” *Phys. Rev. B*, vol. 68, p. 140101, 14 Oct. 2003.
- [22] H. Jiang *et al.*, “Quantitative 3d imaging of whole, unstained cells by using x-ray diffraction microscopy,” *Proceedings of the National Academy of Sciences*, vol. 107, no. 25, pp. 11234–11239, 2010.
- [23] O. Smirnova and M. Ivanov, “Multielectron high harmonic generation: Simple man on a complex plane,” in *Attosecond and XUV Physics*. John Wiley Sons, Ltd, 2014, ch. 7, pp. 201–256, ISBN: 9783527677689. eprint: <https://onlinelibrary.wiley.com/doi/pdf/10.1002/9783527677689.ch7>.
- [24] B. Wang *et al.*, “High-fidelity ptychographic imaging of highly periodic structures enabled by vortex high harmonic beams,” *Optica*, vol. 10, no. 9, pp. 1245–1252, Sep. 2023.
- [25] K. J. Schafer, B. Yang, L. F. DiMauro, and K. C. Kulander, “Above threshold ionization beyond the high harmonic cutoff,” *Phys. Rev. Lett.*, vol. 70, pp. 1599–1602, 11 Mar. 1993.
- [26] P. B. Corkum, “Plasma perspective on strong field multiphoton ionization,” *Phys. Rev. Lett.*, vol. 71, pp. 1994–1997, 13 Sep. 1993.
- [27] R. M. Karl *et al.*, “Full-field imaging of thermal and acoustic dynamics in an individual nanostructure using tabletop high harmonic beams,” *Science Advances*, vol. 4, no. 10, eaau4295, 2018.

- [28] O. A. Sharafeddin, D. J. Kouri, and D. K. Hoffman, "Time-dependent treatment of scattering: Potential referenced and kinetic energy referenced modified Cayley approaches to atom-diatom collisions and time-scale separations," *Canadian Journal of Chemistry*, vol. 70, no. 2, pp. 686–692, 1992.
- [29] D. Attwood and A. Sakdinawat, *X-Rays and Extreme Ultraviolet Radiation: Principles and Applications*, 2nd ed. Cambridge University Press, 2017.
- [30] B. Wang, "Extreme ultraviolet lensless microscopy: Development and potential applications to semiconductor metrology," Ph.D. dissertation, Boulder, 2022/12 2022, p. 140.